JOURNAL OF GEOPHYSICAL RESEARCH, VOL. 92, NO. A13, PAGES 15,234–15,248, DECEMBER 30, 1987

Whistler Mode Emissions in the Uranian Radiation Belts

F. V. CORONITI,[1,2] W. S. KURTH,[3] F. L. SCARF,[1] S. M. KRIMIGIS,[4]
C. F. KENNEL,[1] AND D. A. GURNETT[3]

Voyager 2 detected intense whistler mode emissions and fluxes of energetic electrons during the outbound pass through the region of auroral L shells. The observed energetic ($E > 22$ keV) electron distribution, a model warm ($E < 27.5$ keV) electron distribution, and the cold plasma density profile deduced by Kurth et al. (this issue) are used to calculate the ray path–integrated spatial amplification of whistlers which arrive at Voyager 2 from the magnetic equator. By matching the calculated amplification and the relative gains at different frequencies deduced from the observed whistler power spectrum, the pitch angle anisotropy parameters of the electron distributions are determined to within a fairly narrow range of values. The estimated bounce average pitch angle diffusion coefficient indicates that electrons are on strong diffusion over a wide range in energies. The electron precipitation energy flux is sufficient to produce the observed auroral light emissions.

1. INTRODUCTION

With the Voyager 2 encounter, Uranus has joined the Earth, Jupiter, and Saturn as planets having magnetospheres with trapped radiation belts and plasma wave turbulence. *Krimigis et al.* [1986] reported intense fluxes of energetic ($E > 22$ keV) electrons that peaked just after closest approach and remained high within the "classical" auroral L shell region from $L = 4.8$ to 6–8 (Figures 1 and 2). In addition to high-frequency radio emissions, *Gurnett et al.* [1986] identified whistler mode radiation which occurred as both a steady hiss and, at closest approach, in the form of rising chorus. In Figure 1, whistler emissions begin near spacecraft event time (SCET) 1500 at frequency $f = 560$ Hz, increase in frequency as the electron cyclotron frequency f_c ($=28B$, B in nanoteslas) rises toward closest approach, and reach maximum intensity in the frequency band 311 Hz $< f <$ 1 kHz during the interval SCET 2000–2100. *Gurnett et al.* [1986] remarked that the whistlers should pitch angle scatter energetic electrons and their subsequent precipitation into the Uranian ionosphere might produce the auroral light emissions detected by *Broadfoot et al.* [1986].

In this initial analysis of Uranian whistlers we focus on the interval SCET 2000–2100, where the most intense whistlers were detected and where the strongest pitch angle diffusion and auroral precipitation should occur. Section 2 presents high time resolution measurements of both the whistler emissions and the energetic electron fluxes. In section 3, for two specific times during the SCET 2000–2100 interval, we compute the ray path–integrated spatial gain for whistlers that propagate from the magnetic equator to the Voyager 2 location at moderate magnetic latitudes. The whistler gains are calculated using the observed energetic electron distribution ($E > 27.5$ keV), an inferred warm electron distribution ($E < 27.5$ keV), and the cold plasma density profile deduced by *Kurth et al.* [this issue]. The only free parameters in the gain calculations are the warm and energetic electron anisotropies. We vary the anisotropy parameters until the calculated relative gains at different frequencies match the relative gains deduced from the measured whistler power spectrum. In section 4 we estimate the bounce-averaged electron pitch angle diffusion coefficient and show that the electron fluxes are on strong diffusion over a wide range of energies. The estimated electron precipitation energy flux is sufficient to produce the auroral luminosity measured by *Broadfoot et al.* [1986].

2. AURORAL WAVE-PARTICLE OBSERVATIONS

During the interval SCET 2000–2100, Voyager 2 monotonically traversed the L shell and magnetic dipole latitude (λ) range from $L = 6.3$, $\lambda = 13°$ to $L = 8.95$, $\lambda = 19.5°$ (Figure 2); here and below we have estimated dipole L shell and latitude using the offset tilted dipole (OTD) model of *Ness et al.* [1986]. The magnetic equatorial field strength B_e and electron cyclotron frequency f_{ce} decreased from $B_e = 92$ nT, $f_{ce} = 2575$ Hz at SCET 2000 to $B_e = 32$ nT, $f_{ce} = 900$ Hz at SCET 2100; at the spacecraft the corresponding range of cyclotron frequencies is $f_c = 3230$ (SCET 2000) to $f_c = 1464$ (SCET 2100). In this paper we have used the plasma density model of *Kurth et al.* [this issue], which was deduced by identifying local upper hybrid emissions and $n + \frac{1}{2}$ electron cyclotron harmonic waves. For the time interval SCET 1900–2100, the *Kurth et al.* [this issue] density estimates correspond to the approximate L shell profile

$$N(L) = 2.2(4.8/L)^{1.44} \quad \text{cm}^{-3} \tag{1}$$

where we assumed that the density $N(L)$ was constant along field lines; for the interval SCET 2000–2100 of interest here, the densities given by (1) are consistent with the estimates from the plasma science (PLS) ion data [*McNutt et al.*, 1987]. With this density profile the characteristic magnetic energy per particle, $B_e^2/8\pi N$, varies from 14 keV at SCET 2000 to about 3 keV at SCET 2100, energies which are typical of auroral electrons at Earth.

Figure 3 displays high-resolution (every 4 s) unaveraged electric field spectral amplitudes (volts per meter) from 100 Hz to 10 kHz obtained by the TRW/University of Iowa plasma wave science instrument. *Kurth et al.* [this issue] identified the weak emissions above 3 kHz as $n + \frac{1}{2}$ cyclotron waves. Near

[1]TRW Space and Technology Group, Redondo Beach, California.
[2]Department of Astronomy and Department of Physics, University of California, Los Angeles.
[3]Department of Physics and Astronomy, University of Iowa, Iowa City.
[4]Applied Physics Laboratory, Johns Hopkins University, Laurel, Maryland.

Paper number 7A9031.
0148-0227/87/007A-9031$05.00

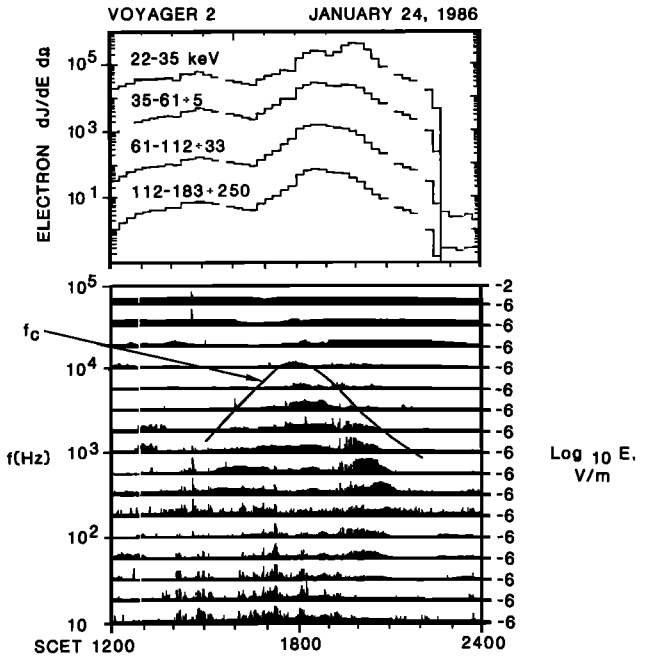

Fig. 1. The top panel displays the electron differential flux (el/cm² s sr keV) measured in four of the LECP channels during the interval SCET 1200–2400; closest approach is near SCET 1800. The 22- to 35-keV flux is given by the scale on the left; the higher-energy fluxes have been divided by the numbers indicated after the energy window for each channel. The bottom panel displays electric field amplitudes (volts per meter) in logarithmically spaced band-pass channels from 10 Hz to 56 kHz. The solid curve represents the value of the electron cyclotron frequency at Voyager 2.

SCET 2000 the intense emissions from 178 Hz to 1.78 kHz are below both the local and equatorial electron cyclotron frequencies and are herein interpreted as waves propagating in the whistler mode; the weak signals at 100 Hz could be very low frequency whistlers but might also be interpreted as lower hybrid emissions excited by the electrostatic ion loss cone instability [*Coroniti et al.*, 1972].

Between SCET 2000 and 2030 the most intense signals occurred in the 562-Hz channel, which corresponds to a normalized frequency $\bar{\omega} = f/f_{ce}$ in the range $\bar{\omega} = 0.22$ (SCET 2000) to $\bar{\omega} = 0.35$ (SCET 2030). Whistler emissions in this normalized frequency range are commonly observed on auroral L shells in both the terrestrial [*Burtis and Helliwell*, 1976] and Jovian [*Inan et al.*, 1983; *Coroniti et al.*, 1984; *Inan*, 1986] magnetospheres; frequently, these whistler signals exhibit the rapid rising (and occasionally falling) frequency structure associated with chorus [*Burtis and Helliwell*, 1969]. Before SCET 2030 the amplitudes of the Uranian whistler emissions fluctuate from measurement to measurement by factors of 3 to greater than 10, which suggests that these signals may also possess the temporally impulsive structure of chorus; unfortunately, Voyager 2 did not obtain any wideband data during this time interval, so that we cannot positively identify the impulsive Uranian signals as chorus.

Near SCET 2030 the 562-Hz amplitudes decrease, and the 311-Hz amplitudes rise to become the dominant emission. For a 311-Hz whistler the normalized frequency varies from $\bar{\omega} = 0.20$ at SCET 2030 to $\bar{\omega} = 0.35$ at SCET 2100. The wave amplitudes become much steadier, suggesting that the whistler emissions have the character of hiss; a Voyager wideband frame obtained at about SCET 2035 [*Gurnett et al.*, 1986] does exhibit a steady, narrow-band emission which resembles terrestrial VLF hiss.

Figure 4 presents four 96-s electric field power spectra from 10 Hz to 56 kHz for selected times during the SCET 2000–2100 period. The lower curves are the 96-s average spectral density, and the upper curves are the peak spectral intensity in each frequency channel during the 96-s interval. On Voyager 2 the frequency channels above 1.0 kHz suffer interference from the spacecraft data system, so that in these high-frequency channels the amplitudes of low-level signals are not accurate. The four spectra are broadly representative of the spectral shapes measured during the SCET 2000–2100 interval. The SCET 2011 spectrum ($L = 6.73$, $\lambda = 13.9°$) exhibits a sharp peak at 562 Hz ($\bar{\omega} = 0.27$) and rapid falloff to both higher and lower frequencies, indicating that the whistler emission is quite

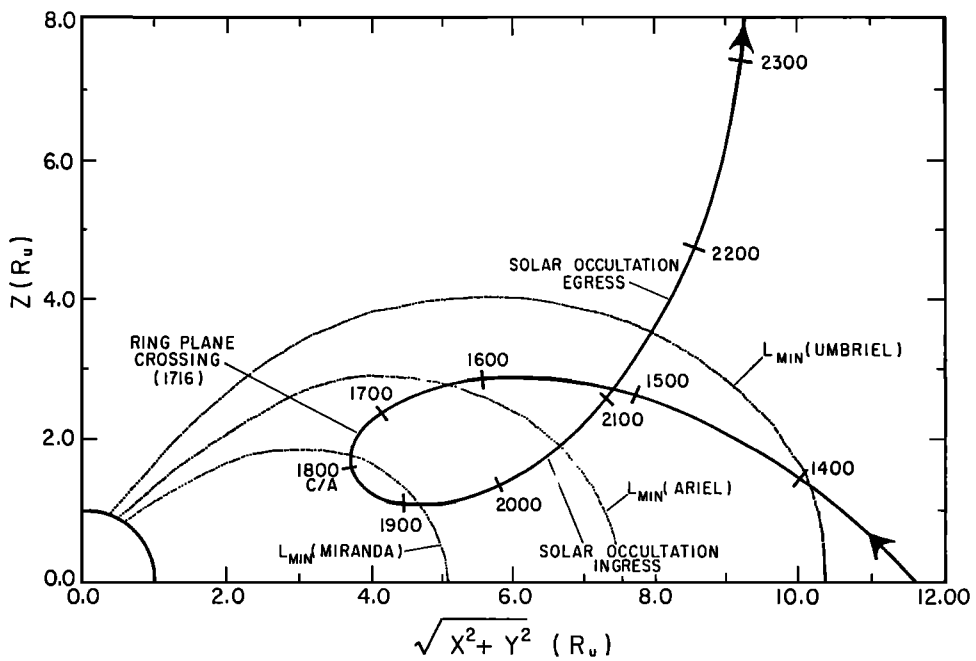

Fig. 2. The trajectory of Voyager 2 projected into a magnetic dipole meridian plane (adapted from *Bridge et al.* [1986]).

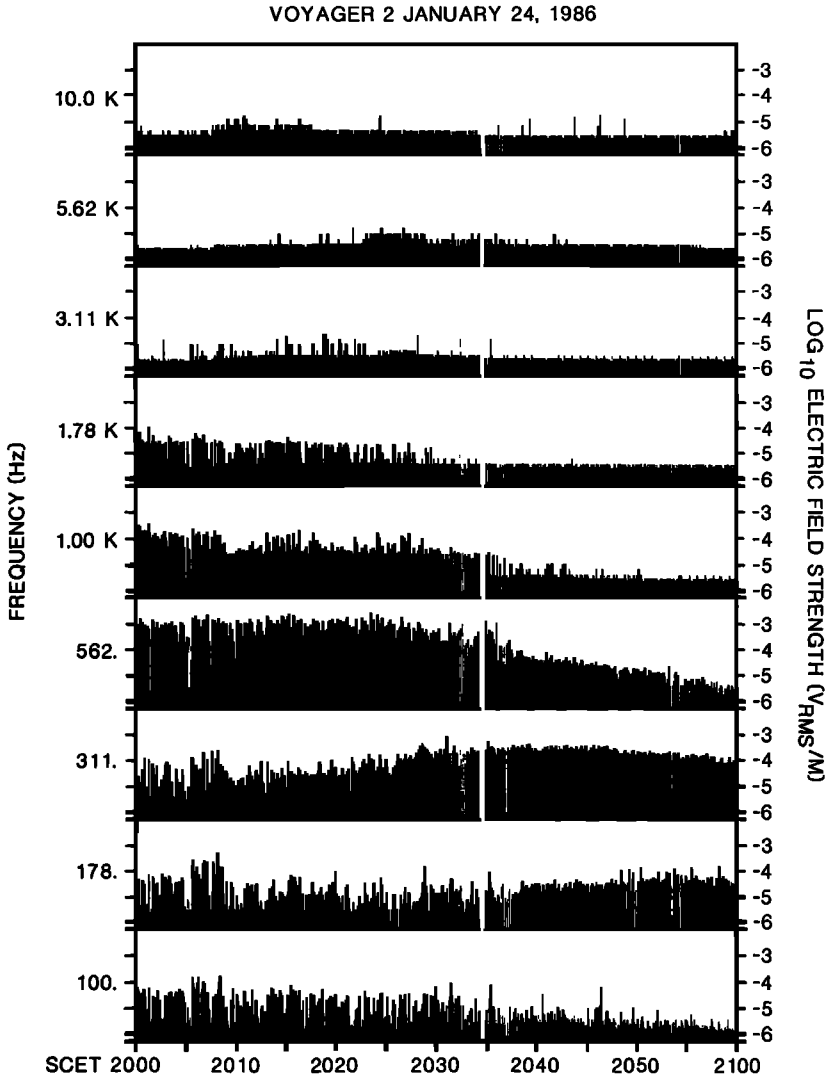

Fig. 3. High-resolution wave electric field amplitudes (volts per meter) from 100 Hz to 10 kHz measured during the interval SCET 2000–2100. Intense whistler emission occurs in the 311-Hz to 1.0-kHz channels. The emissions at 3.11 kHz and above are $n + \frac{1}{2}$ electron cyclotron waves and upper hybrid waves.

narrow banded. A low-intensity, secondary peak occurs near 56–100 Hz, which may indicate a separate emission near the local lower hybrid frequency. At SCET 2027 the substantial enhancement of the 311-Hz ($\bar{\omega} = 0.20$) intensity broadens the spectrum, although 562 Hz ($\bar{\omega} = 0.35$) is still dominant. By SCET 2035 ($L = 7.64$, $\lambda = 16.5°$) the 311-Hz ($\bar{\omega} = 0.215$) average spectral density slightly exceeds the 562-Hz ($\bar{\omega} = 0.39$) intensity, although 562 Hz retains the peak amplitude over the 96-s averaging interval. The emerging dominance of the 311-Hz ($\bar{\omega} = 0.25$) intensity is shown in the SCET 2043 ($L = 8.05$, $\lambda = 17.5°$) spectrum, which exhibits a narrow peak and almost equal peak and average amplitude.

In Plate 1 we show the frequency-time diagram measured by the Voyager wideband system at SCET 2035; during the Uranus encounter, wideband coverage was limited to 10-s snapshots [*Gurnett et al.*, 1986]. No choruslike frequency-time structure is apparent in the wideband intensity, which is therefore consistent with a hisslike emission. We also show an electric field power spectrum obtained by averaging 10 sweeps (0.6 s) of the wideband waveform. Since the Voyager wideband system uses an automatic gain control (AGC) amplifier, only the relative amplitudes at different frequencies are measured. We have calibrated the wideband power spectrum using the E field channel data; hence the displayed spectral densities are only approximate. For reference, at the top of the spectrum we have marked ratios of the frequency to the local electron cyclotron frequency; at the bottom we have marked the ratio of the frequency to the equatorial cyclotron frequency $\bar{\omega}$ on the $7.64L$ shell location of the spacecraft.

The wideband spectrum confirms, at a higher temporal resolution, the relatively broad spectral peak inferred from the lower-frequency resolution channel data of Figure 4 (in the channel measurements a sharp peak could have occurred between 311 Hz and 562 Hz). The frequency bandwidth at a spectral density $1/e$ down from the peak is about 225 Hz, which corresponds to a range of normalized frequencies from $\bar{\omega} = 0.23$ to $\bar{\omega} = 0.39$. At SCET 2035, $B^2/8\pi N = 5.8$ keV. The minimum energy for cyclotron resonance with a parallel propagating whistler is [*Kennel and Petschek*, 1966]

$$E_R = \frac{B^2}{8\pi N} \frac{(1 - \bar{\omega})^3}{\bar{\omega}} \tag{2}$$

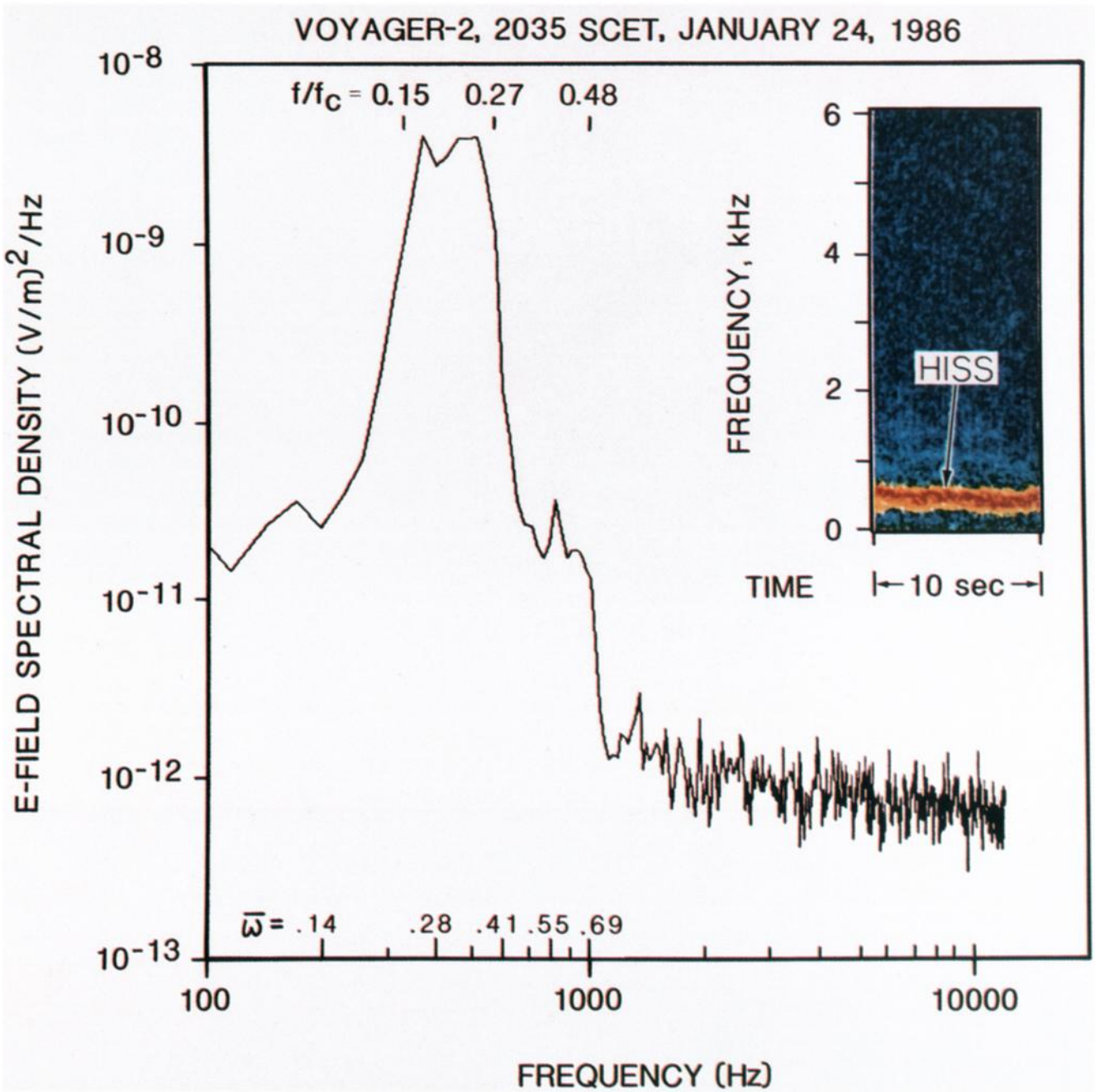

Plate 1. The electric field power spectrum at SCET 2035 obtained by averaging 10 sweeps (= 0.6 s) of the wideband receiver. The wideband system records only the relative power; the spectrum has been calibrated by using the lower time resolution channel measurements. Here f/f_c is the ratio of the wave frequency to the local electron gyrofrequency at Voyager 2; $\bar{\omega}$ is the wave frequency normalized to the equatorial cyclotron frequency of the Voyager 2 L shell ($L = 7.64$). The inset displays the wideband frequency-time diagram from 50 Hz to 6 kHz.

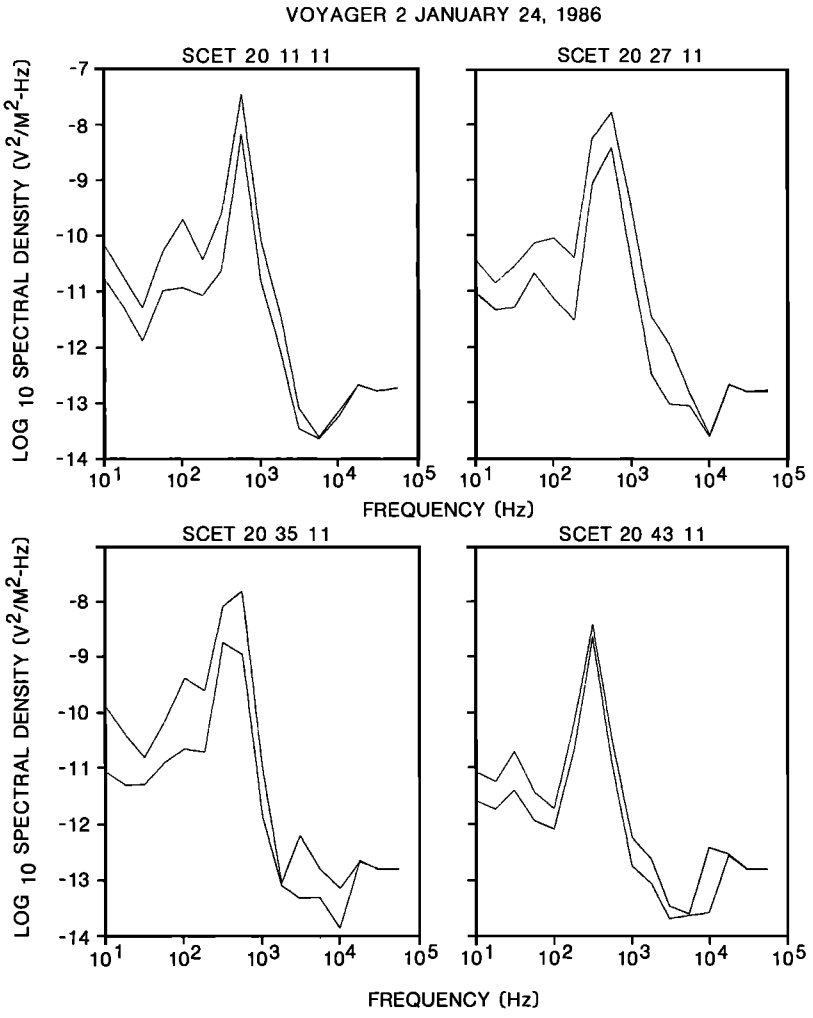

Fig. 4. The electric field power spectral density from 10 Hz to 56 kHz obtained from the digital channel data for four selected intervals. The lower curve is the 96-s average, and the upper curve is the peak spectral density measured during the averaging interval.

Hence the spectral density bandwidth corresponds to equatorial resonance with electrons in the energy range 3.4 keV < E_R < 11.5 keV; at Voyager the local resonant energy is in the range 17 keV < E_R < 44 keV.

Although the intensity in the wideband *f-t* diagram appears to be almost constant, the power spectrum exhibits significant changes on short time scales. Figure 5 shows the superposition of the spectrum in Plate 1 with the two 0.6-s average spectra which immediately precede and follow the Plate 1 spectrum. The high-frequency cutoff near 600 Hz is very steady, but the low-frequency spectral shape and bandwidth are quite variable. The superposed spectra also exhibit a weak emission with peaks near 800 Hz and 1.5 kHz, just below and above the local half cyclotron frequency (~1 kHz) and well above the equatorial half cyclotron frequency.

During the SCET 2000–2100 interval the observed whistlers resonate with electrons over the broad energy range from a few keV to ~100 keV. Unfortunately, during this time, Voyager 2 was within Uranus' shadow, and spacecraft charging complicated the low-energy electron measurements made by the Massachusetts Institute of Technology (MIT) PLS instrument [*Bridge et al.*, 1986]. *Bridge et al.* [1986] have reported intense fluxes of warm 1- to 6-keV electrons, with an omnidirectional integral flux of 2–10 × 10^6 el/cm² s.

The Johns Hopkins/University of Maryland low-energy charged-particle (LECP) experiment measured intense fluxes of electrons in the energy range 22 keV to 1 MeV. Figure 6 displays six successive 8-min average differential energy spectra ($dj/ded\Omega$, in el/cm² s sr keV) from SCET 2004 to 2051 measured at local pitch angles which decreased gradually from $\alpha = 87°$ (SCET 2004) to $\alpha = 77°$ (SCET 2044). Below 150 keV the differential spectra are well fit by a simple power law of the form

$$dj/ded\Omega = j_E t^2 (t_E^2/t^2)^{M+1} (\sin \alpha)^{2A_E} \quad (3)$$

where $t = p/mc$ is the normalized relativistic momentum, t_E corresponds to the central energy of the lowest channel, roughly 27.5 keV, A_E is the pitch angle anisotropy, M is the power law spectral index, and $j_E t_E^2$ is essentially (sin $\alpha \approx 1$) the measured differential flux at t_E. The estimated values of the power law index M are given in the figure, as well as the L shell location of Voyager 2 at the start of each averaging interval. Below 100 keV the differential flux gradually decreased from SCET 2004 to SCET 2051, and M underwent slight variations in the range 1.61 < M < 1.91.

3. Whistler Mode Growth Rates

In this section we interpret the Uranus wave measurements using the standard theory of whistler mode amplification by anisotropic electron distributions [*Kennel and Petschek*, 1966;

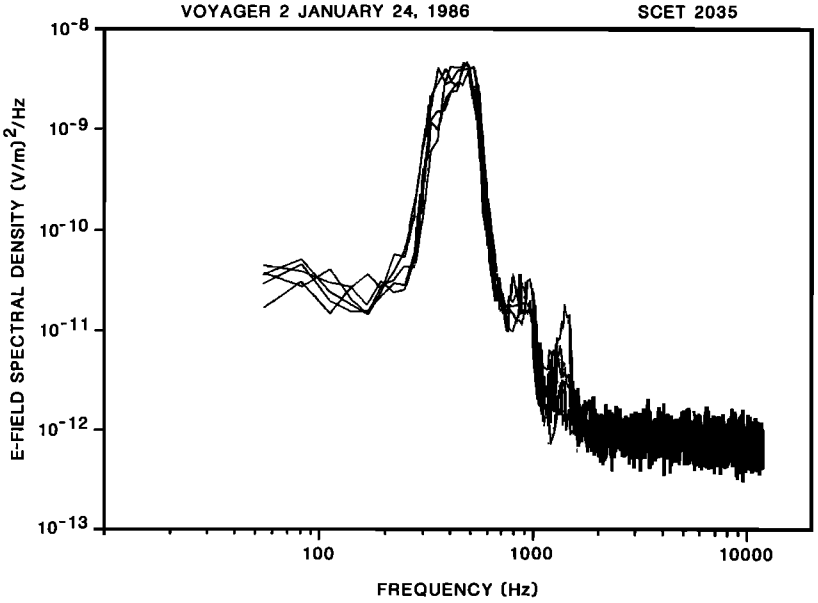

Fig. 5. The superposition of the Plate 1 spectrum and the two 0.6-s average wideband power spectra that immediately precede and follow the spectrum of Plate 1.

Church and Thorne, 1983]. As a whistler propagates along a ray path, the wave electric field amplitude $E(f, s)$ grows exponentially as

$$E(f, s) = E(f, s = 0) \exp\left[G(f, s) = \int_0^s ds\, k_i(f, s)\right] \quad (4)$$

where ds is the differential arc length along the path, $k_i(f, s)$ is the local spatial amplification rate, and $G(f, s)$ is the net gain from the initial location $s = 0$, taken herein as the magnetic equator, to the point s, taken herein as the location of Voyager 2. The initial wave amplitude level $E(f, s = 0)$ is unknown but is definitely not the single particle incoherent fluctuation level [*Church and Thorne*, 1983]; incredibly high exponential gains of 30–40 are needed in order to amplify thermal noise up to the observed wave levels.

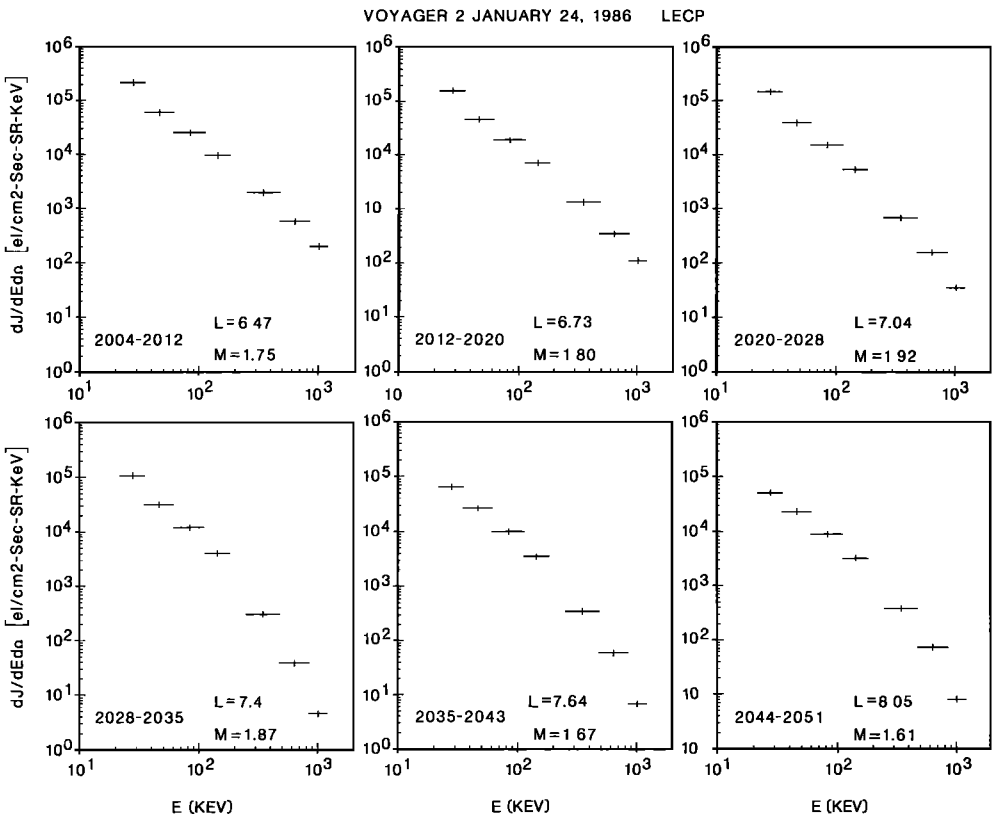

Fig. 6. Six successive 8-min average electron differential flux spectra measured by the LECP detector in the energy range 27.5 keV to 1 Mev. The L shell at the start of each averaging interval and the power law spectral index M are shown for each interval.

Lacking a realistic estimate of $E(f, s = 0)$, we will use the measured Voyager 2 amplitudes $E(f, s)$ to compute the difference in the gain at different frequencies and will match the relative gains to the amplification calculations. Detailed calculations have been carried out for two cases: the SCET 2011 channel spectrum in Figure 4 and the SCET 2035 wideband spectrum in Plate 1. In section 3.1 we describe the model electron distribution functions which are used in the growth rate computations. Section 3.2 briefly outlines a simplified ray path calculation which traces rays that start at the magnetic equator and propagate to the Voyager 2 observation point. Section 3.3 describes the procedure for calculating the wave gain, and section 3.4 presents the comparison of the gain calculations and the wave observations.

3.1. *Model Electron Distributions*

For the energetic electrons above 27.5 keV we convert the observed LECP differential flux into the normalized electron distribution $F(\mathbf{t}) = (mc)f(\mathbf{p})$ as

$$F_E(\mathbf{t}) = \frac{j_E^*(L)mc}{b_*^{A_E}} \left(\frac{t_E^2}{t^2}\right)^{M+1} (\sin \alpha)^{2A_E} \qquad t \geq t_E \tag{5}$$

where $j_E^*(L)$ equals the flux scaling factor of equation (4) (j_E) converted from $(\text{keV})^{-1}$ to $(\text{erg})^{-1}$ and multiplied by the quantity $b_*^{A_E}$, where b_* is the ratio of the local magnetic field strength to the equatorial field strength for the same L shell. Since whistlers propagate across L shells in traveling from their starting location on the equator to Voyager 2, we must specify the L shell dependence of $j_E^*(L)$ and $M(L)$ in order to determine the whistler amplification. For the case study SCET 2011 (SCET 2035), we used the observed differential flux at times SCET 2004, 2012, and 2020 (SCET 2028, 2035, and 2044), obtained from higher time resolution measurements than are shown in Figure 6, to perform a simple quadratic fit for $j_E^*(L)$ in terms of the parameter $L - L_s$ where $L_s = 6.47$ ($L_s = 7.4$); i.e., we took

$$j_E^*(L) = j_E(L_s)b_*^{A}(L_s)g(L - L_s)$$

$$M(L) = M(L_s)h(L - L_s)$$

where g and h are the quadratic fitting functions (see Appendix 1). The functions g and h and the anisotropy factor b^A were incorporated in the calculation of the local spatial growth rate $k_i(s, f)$.

For simplicity, and since we have no observed dependence, we have assumed that the anisotropy A_E is independent of L. On the inbound pass, the pitch angle distributions of the $22 \leq E \leq 35$ keV electrons, which are displayed by *Mauk et al.* [this issue], have an approximate anisotropy $A_E \approx 0.42$ for $L = 6.5$–7.7 and $A_E \approx 0.75$ for $L = 8.8$–9.2. These values are comparable to the estimate of A_E that we obtain below, and they suggest that A_E is not a strong function of L. In our growth rate calculations, whistler ray paths rarely change L shell by more than 0.2–0.3, so that weak anisotropy gradients should not seriously modify our qualitative results; the sensitivity of the calculations to changes in A_E is discussed below.

We do not have electron distribution function measurements for energies below 27.5 keV. We have therefore modeled the warm electron distribution as an anisotropic Maxwellian:

$$F_w(\mathbf{t}) = \frac{j_w^*(L)mc}{b_*^{A_w}} \exp\left[-t^2/t_w^2\right](\sin \alpha)^{2A_w} \qquad t < t_E \tag{6}$$

Requiring $F(t)$ and $\partial F/\partial t$ to be continuous at t_E, we obtain the conditions

$$j_w^* \exp\left[-t_E^2/t_w^2\right] = j_E^*$$
$$t_w^2 = t_E^2/(M + 1) \qquad A_w(t_E) = A_E \tag{7}$$

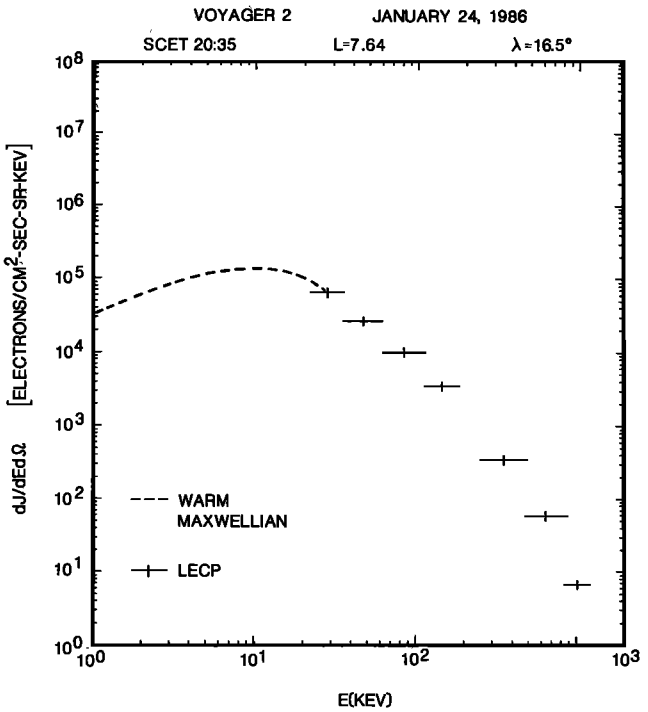

Fig. 7. The modeled warm electron differential flux from 1 keV to 27.5 keV and the measured LECP electron differential flux from 27.5 keV to 1 Mev at SCET 2035. The warm electron distribution is chosen to fit smoothly in energy and pitch angle with the measured energetic electron distribution.

As an example of the combined warm and energetic distribution functions, Figure 7 displays the resulting differential fluxes with $\sin \alpha \approx 1$ for SCET 2035. The warm electron integral flux predicted by the combined model is within a factor of 2 of the flux reported by *Bridge et al.* [1986], so that $F_w(\mathbf{t})$ should provide a reasonable representation of the warm electron distribution.

Parallel whistlers of frequency f are unstable if the pitch angle anisotropy exceeds the critical anisotropy $A_c = f/(f_c - f)$ [*Kennel and Petschek*, 1966]. The sharp decrease in the observed power spectrum for $\bar{\omega} > 0.4$ suggests that the electron anisotropy is of the order of $A \sim 0.6$–0.7. The simplest assumption would be to make the hot and warm electron anisotropies equal. However, in our growth rate computations we found that the observed relative gain at different frequencies could not be explained if $A_w = A_E$. We therefore allowed the warm electron anisotropy to have the following variation with energy,

$$A_w(t) = [A_w(0) - A_E](1 - t^2/t_E^2)^2 + A_E \tag{8}$$

so that $A_w(0)$ is not necessarily equal to A_E but $A_w(t_E) = A_E$ as required by (7); this analytic form of $A_w(t)$ allows the pitch angle distributions of the warm and energetic electron distributions to join smoothly at t_E.

3.2. *Whistler Ray Paths*

In propagating away from the magnetic equator, the whistler wave normal angle undergoes a rapid rotation due to the strong curvature of a dipole magnetic field and gradients in

the wave index of refraction [*Kimura*, 1966; *Thorne and Kennel*, 1967; *Burtis and Helliwell*, 1976]. In the WKB eikenal approximation the equation for the ray path $r(\lambda)$ in a dipole field is

$$\frac{1}{r}\frac{dr}{d\lambda} = \tan(\psi - \phi - \delta) \tag{9}$$

where r is the spherical radius, $\lambda = \pi/2 - \theta$ is the latitude (θ is the colatitude), ψ is the angle between the wave vector $\mathbf{k}$ and the local magnetic field, $\tan\phi = 2\tan\lambda$, and $\tan\delta = (-1/n)\,\partial n/\partial\psi$ [*Stix*, 1962]. In the quasi-longitudinal approximation the whistler index of refraction is

$$n^2 = \frac{f_p^2}{f(f_c\cos\psi - f)} \tag{10}$$

where $f_p = 9(N)^{1/2}$ kHz is the electron plasma frequency; at Uranus the density N is determined by the cold electrons. The angle δ is then given by

$$\tan\delta = \frac{f_c\sin\psi}{2(f_c\cos\psi - f)} \tag{11}$$

In a dipole field the wave normal angle ψ changes with latitude along a ray path according to the equation [*Church*, 1982].

$$\left.\frac{d\psi}{d\lambda}\right|_{\text{path}} = \left[\frac{3n_\theta(1+\sin^2\lambda)}{1+3\sin^2\lambda} - r(\nabla n)_\psi\cdot\hat{\psi}\right]\left[n_\theta - \left(\frac{\partial n}{\partial\psi}\right)_r\psi_\theta\right]^{-1} \tag{12}$$

where $n_\theta = -n\cos(\psi - \phi)$, $\hat{\psi} = \cos(\psi - \phi)\hat{r} + \sin(\psi - \phi)\hat{\theta}$, and $\hat{\psi}_\theta = \hat{\theta}\cdot\hat{\psi}$; $\hat{r}$ and $\hat{\theta}$ are the standard spherical coordinate unit vectors. For a cold plasma density $N(L, \lambda) \propto L^{-q}$ and independent of latitude, equation (12) becomes

$$\left.\frac{d\psi}{d\lambda}\right|_{\text{path}} = \frac{P}{Q} \tag{13a}$$

$$P = 3\cos(\psi - \phi)(1+\sin^2\lambda) + \frac{3}{2}\frac{f_c\cos\psi}{f_c\cos\psi - f}\cdot[\cos(\psi - \phi)(1+3\sin^2\lambda) + \sin(\psi - \phi)\cos\lambda\sin\lambda] + \frac{q}{3}(1+3\sin^2\lambda)\left[\frac{2\sin\lambda\sin(\psi - \phi)}{\cos\lambda} - \cos(\psi - \phi)\right] \tag{13b}$$

$$Q = (1+3\sin^2\lambda)[\cos(\psi - \phi) + \tan\delta\sin(\psi - \phi)] \tag{13c}$$

Equations (9) and (12) are valid if the wave frequency is well above the lower hybrid frequency, a condition which is well satisfied for the frequencies and latitudes of interest here; wave reflection at the lower hybrid requires a more accurate expression for the index of refraction [*Thorne and Kennel*, 1967].

Since we are only interested in wave propagation over the small latitude range $0 \le \lambda \le 16.5°$, we employed a simple finite difference scheme to integrate equations (8) and (12); the integration was accurate to less than 1%. Rays were started at the magnetic equator on an initial L shell L_0 and with an initial wave normal angle ψ_0 such that the wave propagated to the location of Voyager 2.

3.3. *Spatial Growth Rate*

In calculating the net gain along a ray path we retained only the first-order cyclotron resonant and the Landau damping contributions since these interactions are generally the strongest [*Church and Thorne*, 1983]. For the electron distributions (5) and (6) the spatial growth rate $k_i(s)$ is given in Appendix 1. The only free parameters in determining the gain $G(f)$ are the two anisotropies, A_E and $A_w(0)$.

In order to compare with the observed power spectra at SCET 2011 and 2035, we computed $G(f)$ for several frequencies which spanned the peak intensity. For a given observed frequencies f or $\bar{\omega}$, we varied the initial wave normal angle ψ_0 (and correspondingly L_0 and $\bar{\omega}_0$) until $G(f)$ achieved a local maximum. We iteratively adjusted the two anisotropy parameters (A_E and $A_w(0)$) until the difference in the gains of adjacent frequencies closely matched the relative gains deduced from the observed power spectra.

The final "best fit" choice of A_E and $A_w(0)$ is undoubtedly not unique in a mathematical sense. However, because of the sensitive dependence of the spatial growth rate on the anisotropy, small changs in A_E and/or $A_w(0)$ resulted in relatively large changes in the net gain. Since the wave amplitudes depend exponentially on the gain, only very small variations of the anisotropies about the best fit values could be made and still have the relative gains be consistent with the observed amplitudes. Thus, given the basic assumptions in calculating $k_i(s)$, the accuracy of the measured energetic electron fluxes, the model distribution function for the unmeasured warm electrons, and the *Kurth et al.* [this issue] density profile, the best fit anisotropies are rather tightly determined.

3.4. *Results of Gain Calculations*

Figure 8 displays the best fit path-integrated gain as a function of $\bar{\omega}$ (frequency normalized to the equatorial cyclotron frequency of Voyager 2's L shell) for the times SCET 2011 and 2035. The solid dots are the calculated gains which have been maximized for each frequency; these points have been connected by a smooth curve. For the SCET 2011 case, the selected frequencies equal the center frequencies of the Voyager 2 channel spectrum analyzer except for $\bar{\omega} = 0.35$, which falls between the 560-Hz and 1.0-kHz channels. For the SCET 2035 case, the frequencies were chosen to correspond to critical points on the power spectrum of Plate 1. For each of the calculated gains, Table 1 lists the observed frequency $\bar{\omega}$, the initial frequency $\bar{\omega}_0$ (normalized to the equatorial cyclotron frequency on the initial L shell), the initial L shell L_0, the initial equatorial wave normal angle ψ_0, the final wave normal angle ψ_f of the ray at Voyager 2, and the initial (E_0) and final (E_f) cyclotron resonant energy for each wave.

In Figure 8 the crosses represent the amplitude gains determined from the measured Voyager 2 power spectrum by assuming that the gain at the peak of the power spectral density equaled the peak calculated gain. For example, at SCET 2035 (SCET 2011) the observed power at $\bar{\omega} = 0.23$ ($\bar{\omega} = 0.147$) corresponds to an amplitude gain that is 0.66 (2.8) smaller than the gain at $\bar{\omega} = 0.31$ ($\bar{\omega} = 0.265$), the peak of the power spectral density; for the SCET 2011 case, we used the average power spectrum to calculate the relative gains. The anisotropy parameters, A_E and $A_w(0)$, were varied until the differences between the calculated gains and the relative gains inferred from the wave measurements were "sensibly" minimized.

In order to examine the sensitivity of the best fit gains to changes in the anisotropy parameters, Figure 9 displays the gain calculations for the SCET 2035 case in which the energetic electron anisotropy was increased and decreased by 0.1 from the best fit value ($A_E = 0.56$) while holding $A_w(0)$ fixed at

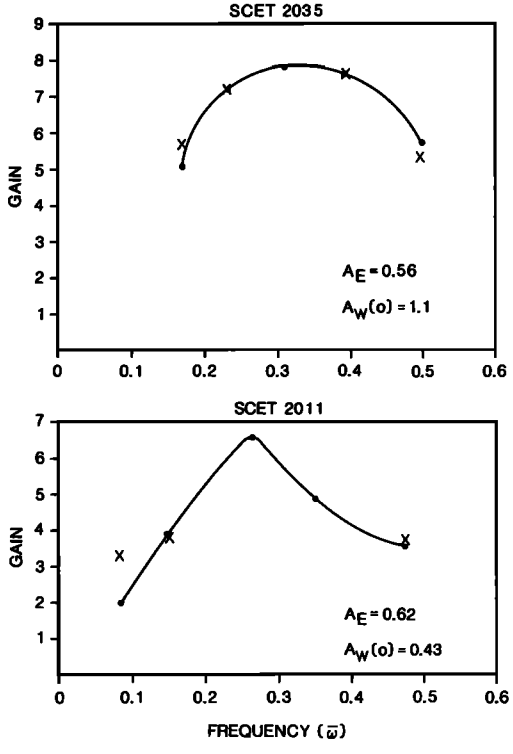

Fig. 8. The calculated ray path–integrated gains at selected frequencies for whistlers starting at the magnetic equator and propagating to Voyager 2 are displayed as points for SCET 2011 and 2035. Each point represents the maximum spatial gain at frequency $\bar{\omega}$ obtained by varying the initial wave normal angle and corresponding initial L shell of each ray. The crosses represent the amplitude gain determined from the measured Voyager 2 power spectrum by assuming that the gain at the peak of the power spectral density equaled the peak calculated gain. The "best fit" anisotropy parameters are $A_E = 0.56$, $A_w(0) = 1.1$ for SCET 2035 and $A_E = 0.62$, $A_w(0) = 0.43$ for SCET 2011.

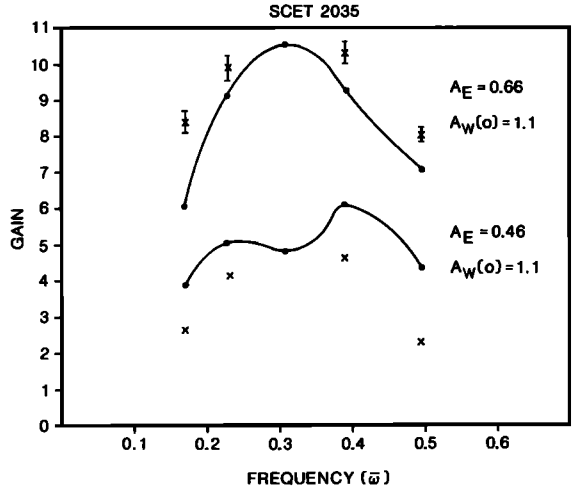

Fig. 9. Calculated gains for A_E increased and decreased by 0.1 from the "best fit" value of 0.56, holding $A_w(0)$ fixed at 1.1. The crosses represent the gains inferred from a power spectrum obtained by averaging the four 0.6–s wideband spectra that immediately precede and follow the SCET 2035 spectra in Plate 1. The error bars in the top graph represent the variance about the average gain which results because of fluctuations in the power spectral density.

its best fit value. The crosses correspond to the gains inferred by averaging the Plate 1 spectrum with the four spectra that immediately precede and follow (see Figure 5) the Plate 1 spectrum. The error bars attached to the crosses in the $A_E = 0.66$ plot represent the variance about the gain inferred from the average power spectral density. Clearly, even including the variances, neither the $A_E = 0.66$ nor the $A_E = 0.46$ gain provides a reasonable fit to the measured power spectrum. Figure 10 displays the gains calculated by increasing and decreasing $A_w(0)$ by 0.2 from the best fit value ($A_w(0) = 1.1$) while holding A_E fixed at its best fit value (note the different scales for the two cases). Changing $A_w(0)$ has little effect on the gain of the two lowest frequencies but significantly alters the gain at high frequencies. Although the $A_w(0) = 0.9$ case is not an unreasonable fit to the inferred gains, the gains near the spectral peak are more closely matched for $A_w(0) = 1.1$.

An interesting feature of the gain calculation is the large initial wave normal angles of the waves with frequencies above that of the maximally growing mode. For nearly parallel propagation at the equator these higher-frequency modes are either damped or only weakly growing for the best fit anisotropy parameters (the actual anisotropy is neither A_E nor $A_w(0)$ but a complicated weighted average over the distribution function). The highly oblique higher-frequency waves are more strongly unstable at the equator and thus have the larger path-integrated gains. If we had considered only nearly parallel waves at the equator, a significantly larger anisotropy would have been required in order to have appreciable wave growth for $\bar{\omega} \sim 0.4$–0.5. It would then have been impossible for the integrated gain to maximize at the observed frequencies of $\bar{\omega} = 0.265$ (SCET 2011) and $\bar{\omega} = 0.31$ (SCET 2035), since the growth rate of parallel whistlers peaks for frequencies just below $A/1 + A$. Furthermore, for parallel whistlers the frequency bandwidth about the maximally growing mode is quite narrow, which would, after spatial amplifi-

TABLE 1. Ray Tracing Parameters

f, Hz	$\bar{\omega}$	$\bar{\omega}_0$	L_0	ψ_0	ψ_f	E_0, keV	E_f, keV
			SCET 2011 ($L = 6.73$)				
178	0.084	0.085	6.745	−25	26.05	90.5	180.0
311	0.147	0.1475	6.737	−25	27.54	43.24	94.1
560	0.265	0.2644	6.725	−25	30.9	15.8	39.2
740	0.35	0.347	6.71	−60	−46.0	7.6	24.8
1000	0.473	0.414	6.44	−60	−47.3	3.5	8.6
			SCET 2035 ($L = 7.64$)				
245	0.17	0.16	7.496	−20	43.2	23.5	65.0
334	0.23	0.2185	7.51	−20	45.0	13.8	42.4
447	0.31	0.296	7.54	−20	47.8	7.3	26.7
560	0.388	0.3985	7.71	−55	−25.5	2.6	16.6
716	0.496	0.45898	7.446	−55	−25.67	1.4	7.5

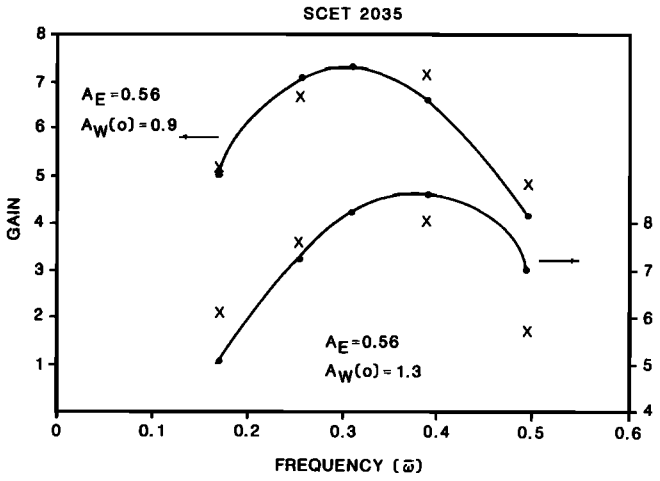

Fig. 10. Calculated gains for $A_w(0)$ increased and decreased by 0.2 from the "best fit" value of 1.1, holding $A_E = 0.56$. The crosses are the gains inferred from a power spectrum obtained by averaging the 0.6-s wideband spectra that immediately precede and follow the SCET 2035 spectrum.

cation, produce a very narrow band emission (typically $\Delta\bar{\omega} < 0.1$). It was the observed relatively broad band spectrum which led us to consider highly oblique propagation.

3.5. *Discussion*

The above gain calculations indicate that the Voyager 2 wave spectra can be explained reasonably well by the spatial amplification of whistlers. Nevertheless, some caution is in order. Changing the electron distributions and/or the cold density profile will result in significant (but probably modest) changes in the best fit anisotropy parameters and the characteristic parameters ($\bar{\omega}_0$, ψ_0, L_0) of the maximally growing waves. Furthermore, we assumed that the observed wave spectrum was dominated by waves that commenced amplification at the magnetic equator. Although perhaps reasonable for a first attempt, this assumption is undoubtedly an oversimplification, and the actual waves which make up the observed spectrum probably have a wide range of initial starting locations and complex ray trajectories. Hence our gain calculations are probably best viewed as indicating a general and a broad consistency between the Voyager 2 wave observations and the whistler amplification model.

4. DIFFUSION LIFETIMES AND PRECIPITATION FLUXES

In the standard whistler turbulence theory [*Kennel and Petschek*, 1966; *Thorne*, 1983] the stably trapped limit flux is usually obtained by requiring that the wave power exponentiate a few times (typically three) as a wave transits the unstable equatorial region. Since the calculated gains in the previous section are somewhat larger, we should expect that the Uranian electron fluxes are near or on strong diffusion [*Kennel*, 1969]. In section 4.1 we estimate the whistler pitch angle diffusion coefficient $D_{\alpha\alpha}$ and the electron scattering times T_S. For simplicity, we assume that the observed whistler spectrum at Voyager 2 is representative of the wave power spectrum throughout the equatorial region. Since the wave vector spectrum is not known, we further assume that $D_{\alpha\alpha}$ is reasonably approximated by the diffusion coefficient for parallel whistlers; thus we ignore diffusion from Landau and higher-order cyclotron resonances [*Lyons et al.*, 1972] and consequently obtain an upper bound on the scattering time. In section 4.2 we estimate the electron precipitation fluxes.

Earlier, we suggested that the impulsive emissions detected before SCET 2030 might be chorus; consequently, the applicability of the quasi-linear theory might be questioned for such structured emissions. *Inan* [1986] has shown that the precipitation flux induced by an isolated chorus element is in general agreement with the fluxes estimated by quasi-linear theory. Furthermore, since electrons bounce many times before being scattered into the loss cone, their interaction with even isolated chorus elements will have an average diffusive character. Finally, the continuity of the Uranian whistler emissions suggests that they may resemble the Jovian chorus; except for a few isolated cases (which *Inan et al.* [1983] analyzed) the Jovian chorus elements were temporally tightly packed and even overlapping. For such chorus the quasi-linear estimate of the diffusion coefficient will be quite accurate.

4.1. *Scattering Times*

The pitch angle diffusion coefficient for parallel whistlers can be written as [*Coroniti et al.*, 1980]

$$D_{\alpha\alpha} = \frac{e^2 B^2(f)}{8m^2c^2\gamma^2}\left|\frac{v_g}{v_g + |v_\parallel|}\right|_{\omega=\omega_r} \tag{14}$$

where v_g is the group, $B^2(f)$ is the magnetic power spectral density (G^2/Hz) for positive frequencies, and all quantities are evaluated at the resonant frequency where $\gamma(\omega_r - k_\parallel(\omega_r)v_\parallel) - \Omega = 0$. Since the assumption of parallel whistler interactions provides only a rough estimate of the actual diffusion rate, we will neglect relativistic corrections in the following discussion ($\gamma \approx 1$) and use the analytically simpler nonrelativistic relations between wave frequency and resonant energy (equation (2)). For the maximum energy of interest ($E \sim 150$ keV), $\gamma \sim 1.3$. Hence the neglect of γ in (14) results in the scattering lifetime (below) being underestimated by about 70%; at lower energies the correction is negligible. If we convert from $B(f)$ to the measured electric field spectral amplitude $E(f)$ using

$$B(f)(\text{nT/Hz}^{1/2}) = (10n/3)E(f)(\text{V/m} - \text{Hz}^{1/2})$$

(14) becomes

$$D_{\alpha\alpha} = 4.4 \times 10^4 n^2 E^2(f)\left|\frac{v_g}{v_g - |v_\parallel|}\right|_{\omega=\omega_r} \tag{15}$$

As an electron traverses the equatorial region, it resonates with whistlers of different frequencies. Since the observed $E^2(f)$ depends rather strongly on frequency, we calculate the bounce average of $D_{\alpha\alpha}$ as

$$\bar{D}_{\alpha\alpha} = \frac{\int_0^l dS/v_\parallel\, D_{\alpha\alpha}}{\int_0^l dS/v_\parallel} \sim \frac{1}{l}\int_0^l dS\, D_{\alpha\alpha} \tag{16}$$

where $l \approx \pi L R_U/2$ is one-half the length of a dipole line of force; in (16) we have neglected the spatial dependence of $v_\parallel$ since $v_\parallel$ varies only slightly across the resonant region. The details of calculating $\bar{D}_{\alpha\alpha}$ for the observed $E^2(f)$ at SCET 2011 and 2035 are discussed in Appendix 2. The average pitch angle scattering time as a function of particle energy is roughly given by $T_S \approx 1/\bar{D}_{\alpha\alpha}$. The electron fluxes will be on (or near)

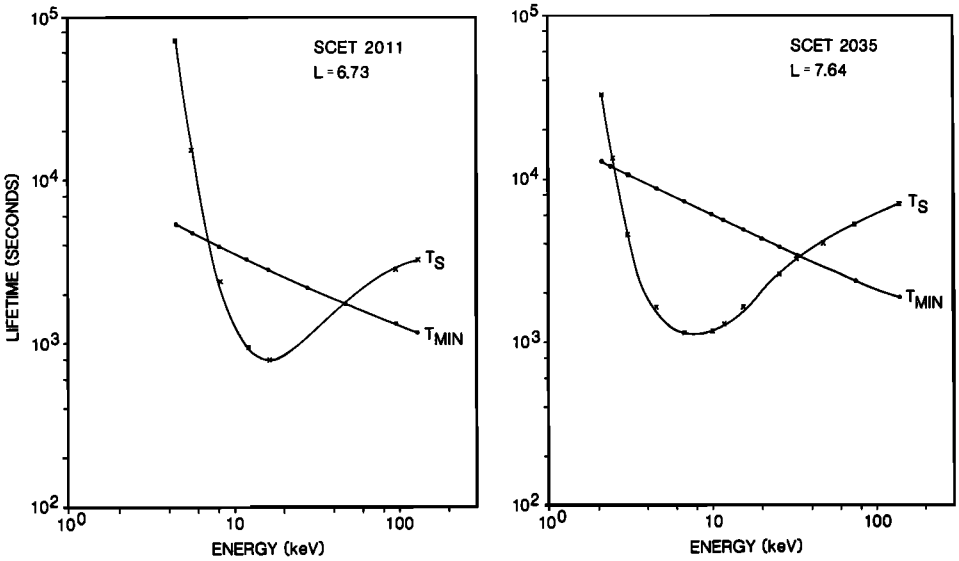

Fig. 11. The scattering time T_S, calculated from the bounce-averaged pitch angle diffusion coefficient, and the minimum precipitation lifetime T_{min} against energy (keV) for SCET 2011 and 2035. The energy range for which $T_S < T_{min}$ should be precipitating at the strong diffusion limit.

the strong diffusion limit when $T_S < T_{min}$, where

$$T_{min} = \frac{4L^4 R_U}{v_\parallel} \tag{17}$$

is the minimum precipitation lifetime [*Kennel*, 1969].

Figure 11 displays the scattering time T_S and the minimum lifetime T_{min} as a function of the minimum energy for cyclotron resonance at the equator for the two cases SCET 2011 ($L = 6.73$) and SCET 2035 ($L = 7.64$). For SCET 2011 (SCET 2035), electrons in the energy range 7 keV $< E <$ 48 keV (2.5 keV $< E <$ 35 keV) have $T_S < T_{min}$ and should therefore be on strong diffusion. For lower energies, T_S rapidly becomes very large, a consequence of the sharp falloff of the whistler power spectrum with increasing frequency. At higher energies, T_S increases less rapidly, even though the power spectrum also diminishes sharply with decreasing frequency. As they travel away from the equator, higher-energy electrons can resonate with the peak spectral intensity and thus have a smaller scattering time than would be inferred from the equatorial resonant frequency.

The importance of bounce-averaging $D_{\alpha\alpha}$ can be illustrated, using the SCET 2035 case, by considering a 20-keV electron which at the equator resonates with an $\bar{\omega} = 0.17$ whistler. The equatorial value of the diffusion coefficient is $D_{\alpha\alpha}{}^e = 1.15 \times 10^{-4}$. Suppose we estimate $\bar{D}_{\alpha\alpha}$ in the usual way by taking $\bar{D}_{\alpha\alpha} = (\Delta l/l) D_{\alpha\alpha}{}^e$ where Δl is the length of the resonant region. For $\Delta l/l = 2^{1/2}/3\pi$ (see equation (A16)), which corresponds to a latitude interval of about 14°, we find $\bar{D}_{\alpha\alpha} \approx 1.7 \times 10^{-5}$ and $T_S \approx 6 \times 10^4$ s and would conclude that the 20-keV electrons are on weak diffusion. The bounce-averaged T_S is equal to 2×10^3 s and is less than the minimum lifetime. Hence off-equatorial resonant interactions can dramatically reduce the lifetimes of higher-energy electrons whenever the power spectrum is strongly peaked in frequency.

4.2. *Precipitation Fluxes*

The electron precipitation flux J_p into the atmosphere is related to the trapped flux J_T by the approximate scaling [*Coroniti and Kennel*, 1970]

$$\frac{J_P}{J_T} = \frac{T_{min}}{T_L} \tag{18}$$

where T_L is the electron lifetime. On strong diffusion ($T_S < T_{min}$), $T_L \approx T_{min}$. The ratio of the precipitation to trapped energy fluxes also scales roughly as T_{min}/T_L. For SCET 2011 and 2035, Table 2 lists the electron precipitation and energy fluxes obtained by integrating over the energy range in which $T_S < T_{min}$; we separately computed the respective contributions of the warm and energetic electrons. The total precipitation energy flux increases from 0.5 erg/cm² s at $L = 7.64$ to 1.0 erg/cm² s at $L = 6.73$. On the outbound pass, intense whistler emissions were detected from SCET 1950 ($L \approx 6$) to SCET 2100 ($L \approx 9$). Since the energetic electron fluxes increased slowly with decreasing L shell during this period, the peak precipitation energy flux could have exceeded 1.0 erg/cm² s at somewhat lower L shells than $L = 6.73$.

Broadfoot et al. [1986] reported the frequent detection of auroral luminosity which was consistent with emission from

TABLE 2. Precipitation Fluxes

Parameter	Value
SCET 2011 ($L = 6.73$)	
Warm electrons: 7 keV $< E <$ 27.5 keV	
Precipitation flux, el/cm² s	1.6×10^7
Energy flux, ergs/cm² s	0.44
Energetic electrons: 27.5 keV $< E <$ 48 keV	
Precipitation flux, el/cm² s	9.85×10^6
Energy flux, ergs/cm² s	0.54
SCET 2035 ($L = 7.64$)	
Warm electrons: 2.5 keV $< E <$ 27.5 keV	
Precipitation flux, el/cm² s	2.3×10^7
Energy flux, ergs/cm² s	0.18
Energetic electrons: 27.5 keV $< E <$ 35 keV	
Precipitation flux, el/cm² s	3.9×10^6
Energy flux, ergs/cm² s	0.27

the south magnetic pole. From the observed UV fluxes they estimated a total precipitation power from electrons in the 10-keV energy range of 2×10^{11} W, assuming a uniformly illuminated 20° polar cap (area: 2.5×10^{18} cm^2). Hence the UV emissions require an average auroral precipitation energy flux of ~ 0.8 erg/cm^2 s, which is consistent with the precipitation fluxes calculated from the observed whistler turbulence.

5. Discussion

The observed intense whistler emissions and the relatively high fluxes of warm and energetic electrons indicate that the Uranian magnetosphere does possess a "classic" auroral zone in which strong wave-particle pitch angle scattering precipitates electrons into the atmosphere. The Voyager 2 power spectra at SCET 2011 and 2035 can be reasonably well explained by the spatial amplification of whistlers using the observed energetic and inferred warm electron fluxes and the *Kurth et al.* [this issue] cold density profile. (Actually, in attempting to fit the observed whistler spectra we independently concluded that the cold plasma density at SCET 2011 and 2035 had to be very close to the *Kurth et al.* [this issue] values; small deviations from these values result in relative gains that deviate significantly from those inferred from the wave observations.) The amplification calculations depended only on the two anisotropy parameters which are rather tightly constrained in order to reproduce the observed spectral shapes. However, we must emphasize that the amplification model is undoubtedly oversimplified, and thus we have demonstrated only a broad consistency between theory and observations. Over a fairly wide range in energy the observed whistler amplitudes will maintain the electron fluxes on strong diffusion. Estimates of the electron precipitation energy flux are comparable to those derived from the UV observation of Uranian aurorae.

The high wave-particle activity observed from $L = 6$ to 9 on the outbound pass is in distinct contrast to the modest whistler and electron flux levels which were detected on Voyager 2's inbound transit through the same L shell region but at slightly larger magnetic latitudes (roughly SCET 1500–1730, $16° < \lambda < 32°$). During this inbound interval the plasma density was apparently very low ($N < 0.1$ cm^{-3}) [*Selesnick and McNutt*, this issue; *Kurth et al.*, this issue]. Hence at $L \sim 7$, $B^2/8\pi N > 100$ keV at the equator, and the observed high-energy electron fluxes are likely to be below the stably trapped limit.

The strong precipitation losses which are inferred from the observed outbound whistler intensities pose several conundrums. In a minimum lifetime an electron of energy E undergoes a magnetic gradient drift of the order of

$$\phi_M = 7.5°(L/7.5)^5(E/27 \text{ keV})^{1/2}$$

in magnetic longitude. During the interval SCET 1950–2100 of intense whistler emissions, Voyager 2 moved approximately 20° in magnetic longitude in a direction opposite to the gradient drift, and Uranus rotated through an angle of about 24°. Hence the spatial region of strong losses probably has a minimum extent of some 20°–25° in longitude, and electrons are unlikely to drift out of this region before suffering a severe flux depletion. The apparent implication of this line of reasoning is that there must have existed a strong source of 5- to 40-keV electrons in order to maintain the fluxes on strong diffusion on time scales longer than $T_{\min}$.

Both *Mauk et al.* [this issue] and *Cheng et al.* [this issue] have presented evidence for the temporal variability of the Uranian energetic proton and electron fluxes and have speculated that substormlike injections may be occurring in the radiation belts. The observed factor of 10 enhancement of the outbound to inbound $22 < E < 35$ keV electron fluxes may be evidence for unsteady injection and/or acceleration processes; the observed pitch angle anisotropy of the inbound fluxes can account for only a factor of 2 reduction from the outbound flux due to the higher magnetic latitude of the inbound pass.

Cheng et al. [this issue], however, present an argument against strong temporal variability. They compare the inbound and outbound phase space densities near $L \sim 9$–10 where Voyager provided measurements at the same first and second adiabatic invariant. Although the electron phase space densities decrease with L, indicating losses, the inbound and outbound values are nearly equal at all energies, which suggests azimuthal drift symmetry and the absence of significant injections. The observed whistler intensities near $L \sim 9$–10 are low, which is consistent with weak precipitation losses. However, outbound near $L \sim 9$–10, the cold density N is about 2–3 cm^{-3} [*McNutt et al.*, 1987], so that $B^2/8\pi N \lesssim 1$ keV. The strong losses could have reduced the fluxes to near the stable trapping limit; at $L = 9$ the stably trapped flux is $\sim 3 \times 10^6/(A - A_c)$ el/cm^2 s, which could be comparable to the observed flux of $\sim 7 \times 10^6$ el/cm^2 s. The long minimum lifetimes at $L \sim 9$–10, however, suggest that convective and/or radial diffusive transport may provide a more rapid loss of electrons than does precipitation.

Another difficulty for the possible occurrence of strong diffusion losses in the $6 < L < 9$ region concerns *Cheng et al.*'s [this issue] estimates of the radial diffusion coefficient. *Cheng et al.* [this issue] argue that the absence of satellite sweeping signatures, which are theoretically possible [*Paonessa and Cheng*, 1987], indicates that the radial diffusion coefficient D_{LL} must exceed the satellite loss time at the minimum Ariel L shell; using both the electron and proton phase space density profiles, they find $D_{LL} \sim 10^{-6} - 10^{-7}$ s^{-1} at $L \sim 7.5$. In order to balance strong diffusion losses we require $D_{LL} T_{\min} \gtrsim 1$ or $D_{LL} \sim 2.5 \times 10^{-4}$ s^{-1} for $E \gtrsim 27.5$ keV electrons, a value that is much higher than found at Jupiter and Saturn. In addition, solar wind driven convection is inadequate to transport electrons to $L \sim 6$–7 against strong diffusion losses even if the full solar wind electric potential is imposed across the magnetosphere. Hence rapid inward transport that can maintain the electron fluxes against strong losses appears difficult to achieve on an auroral L shell at Uranus.

Given that the evidence for substormlike injections and rapid radial transport is not conclusive, we should ask whether the precipitation lifetime calculations can be in error. The pitch angle diffusion coefficient depends on the whistler magnetic field spectral density, which is not measured by the Voyager wave instrument. We calculated the whistler magnetic amplitude from the measured electric field spectrum, a step that involves several assumptions: (1) all the E field intensity is due to whistler mode emissions; (2) the E field signals are primarily transverse to the dc magnetic field; and (3) the index of refraction (essentially the plasma density) is known. The only defense of the first two assumptions is an appeal to previous experience. For the third, the three independent estimates (see *McNutt et al.* [1987], *Kurth et al.* [this issue], and the growth rate analysis of this paper) of the plasma density during the SCET 2000–2100 interval are essentially in agreement. In calculating the bounce-averaged diffusion coefficient we further assumed that the whistler emissions existed

throughout the $\pm 16°$ region about the magnetic equator. Since the ray tracing amplification calculations are reversible as to direction of wave propagation, their success in explaining the observed Voyager E field spectra, and previous experience with whistler emissions, strongly suggest that the whistler wave amplitudes occur throughout the equatorial region. Finally, in order for the calculated scattering lifetimes to imply strong precipitation losses, the diffusion rate must be maintained along the drift and/or radial transport trajectory of an electron for a time comparable to $T_{\min}$. If the wave amplitudes and/or the plasma density are spatially inhomogeneous or temporally variable, the actual scattering times could considerably exceed the calculated T_S based on local wave measurements. However, the long temporal duration over a $\sim 20°$ longitude region of the observed wave activity argues against strong spatial and temporal inhomogeneities. Hence the above considerations suggest that the calculated scattering times are probably reasonable and that the electron precipitation losses were on strong diffusion.

A possible interesting consequence of the short whistler scattering times is that low-energy electrons could undergo a significant upward diffusion in energy before being lost to the atmosphere. *Kennel* [1969] showed that when $T_S/T_{\min} < 1$, a delta function source at low energies would quasi-linearly diffuse into a high-energy tail of the form

$$f(E) \propto E^{-3/8} \exp\left[-(E/E_0)^{5/4}\right]$$

where

$$E_0 = \left[\frac{25}{4}\frac{T_{\min}(E = B^2/8\pi N)}{T_S}\right]^{2/5}\left(\frac{B^2}{8\pi N}\right)$$

From Figure 11 we have $T_{\min}/T_S \sim 2$–5 for the strongly scattered energy range. Hence $E_0 \sim (2.7 - 4.0)B^2/8\pi N$, which yields $E_0 \sim 27$–40 keV ($L = 6.73$) and $E_0 \sim 16$–24 keV ($L = 7.64$). Since the functional form of the accelerated electron distribution undoubtedly depends on details of the whistler wave spectrum that were not included in *Kennel*'s [1969] rough calculation, a direct comparison of the above quasi-linear $f(E)$ and the observed Voyager electron energy spectrum is probably unwarranted. However, the scaling energy E_0 should represent a characteristic energy of the whistler accelerated electrons. Hence whistler energy diffusion is a possible source of the 10- to 40-keV electrons observed on the Uranian auroral L shells.

In conclusion we arrive at no conclusions on the origin and transport of the Uranian radiation belts. The calculated whistler scattering times are likely correct. The implied strong diffusion losses are difficult to reconcile with the observed behavior of the electron phase space densities which indicate only weak radial diffusion and "substormlike" injections. Perhaps whistler turbulence or other processes (such as parallel electric fields) accelerate electrons within the auroral region. The magnetospheric radiation belt adventure continues.

APPENDIX 1

The general expression for the whistler temporal growth rate ω_i can be found in the work by *Church and Thorne* [1983]. In our calculations we have retained only the Landau and first-order cyclotron resonant contributions. We have converted the temporal growth rate to the spatial growth rate k_i through the relation $k_i = \omega_i/v_g$; the whistler group speed is

$$v_g = \frac{2c\Omega_0\bar{\omega}_0^{1/2}[b\cos\psi - \bar{\omega}_0]^{3/2}(1 + \tan^2\delta)^{1/2}}{\omega_p b} \tag{A1}$$

where Ω_0 is the equatorial cyclotron frequency corresponding to the initial L shell (L_0), $\bar{\omega}_0 = \omega/\Omega_0$, $b = B(L, \lambda)/B(L_0, 0)$ is the ratio of the local field strength to the equatorial field strength on the initial L shell, and ω_p is the local electron plasma frequency.

For the electron distribution (4) and (5), the cyclotron resonant contribution to k_i is

$$\begin{aligned} k_C = {} & \frac{\pi^2 j_E^* m\Omega_0}{N}\frac{(b - \bar{\omega}_0)^2\cos\delta}{\cos\psi\,(b\cos\psi - \bar{\omega}_0)} \\ & \cdot\left\{\frac{1}{b_*^{A_E}}\int_{\max(t_E,t_c)}^{\infty} dt\, t\left(\frac{t_E^2}{t^2}\right)^{M+1}(\sin\alpha_c)^{2A_E}\right. \\ & \cdot\left[\frac{A_E b}{\gamma\bar{\omega}_0} - (M + 1 + A_E)\sin^2\alpha_c\right] \\ & \cdot\left[\frac{(1 + \cos\psi)J_0}{2} - \frac{\bar{\omega}_0(b - \gamma\bar{\omega}_0)\sin\psi\tan\psi\tilde{J}_1}{b(b - \bar{\omega}_0)}\right]^2 \cdot \\ & + \exp\left(\frac{t_E^2}{t_w^2}\right)\int_{\min(t_E,t_c)}^{t_E} dt\, t\,\frac{\exp(-t^2/t_w^2)(\sin\alpha_c)^{2A_w}}{b_*^{A_w}} \\ & \cdot\left[\frac{A_w b}{\bar{\omega}_0} - \left(\frac{t^2}{t_w^2} + A_w - \frac{t}{2}\frac{\partial A_w}{\partial t}\ln\left(\frac{\sin^2\alpha_c}{b_*}\right)\right)\sin^2\alpha_c\right] \\ & \cdot\left.\left[\frac{(1 + \cos\psi)J_0}{2} - \frac{\bar{\omega}_0\sin\psi\tan\psi\tilde{J}_1}{b}\right]^2\right\} \end{aligned} \tag{A2}$$

In (A2), $A_w = A_w(t)$, and $\gamma = (1 + t^2)^{1/2}$ is the relativistic Lorentz factor. $J_0(x)$, $\tilde{J}_1(x) = xJ_1(x)$ are Bessel functions of argument $x = k_\perp p_\perp/m\Omega$. The minimum momentum for cyclotron resonance is

$$t_c = \frac{b}{\bar{\omega}_0(n_\parallel^2 - 1)}\left[n_\parallel - \left(1 + \frac{\bar{\omega}_0^2(n_\parallel^2 - 1)}{b^2}\right)^{1/2}\right] \tag{A3}$$

where $n_\parallel = n\cos\psi$. The pitch angle at which cyclotron resonance occurs is

$$\cos\alpha_c = \frac{\gamma\bar{\omega}_0 - b}{\bar{\omega}_0 n_\parallel t} \tag{A4}$$

The contribution to k_i from the Landau resonant interaction is

$$\begin{aligned} k_L = {} & -\frac{2\pi^2 j_E^* m\Omega_0}{N}\frac{\bar{\omega}_0^2\tan\psi\sin\delta}{b} \\ & \cdot\left\{\frac{(M + 1 + A_E)}{b_*^{A_E}}\int_{\max(t_E,t_L)}^{\infty} dt\, t\left(\frac{t_E^2}{t^2}\right)^{M+1}(\sin\alpha_L)^{2A_E}\cos^2\alpha_L\right. \\ & \cdot\left[J_0 - \gamma\frac{b\cos\psi - \bar{\omega}_0}{b\cos\psi}\tan^2\alpha_L\tilde{J}_1\right]^2 \\ & + \exp\left(\frac{t_E^2}{t_w^2}\right)\int_{\min(t_E,t_L)}^{t_E} dt\, t\,\frac{\exp(-t^2/t_w^2)(\sin\alpha_L)^{2A_w}\cos^2\alpha_L}{b_*^{A_w}} \\ & \cdot\left[\frac{t^2}{t_w^2} + A_w - \frac{t}{2}\frac{\partial A_w}{\partial t}\ln\left(\frac{\sin^2\alpha_L}{b_*}\right)\right] \\ & \cdot\left.\left[J_0 - \frac{b\cos\psi - \bar{\omega}_0}{b\cos\psi}\tan^2\alpha_L\tilde{J}_1\right]^2\right\} \end{aligned} \tag{A5}$$

In (A5) the Landau resonant momentum is

$$t_L = \frac{1}{(n_\parallel{}^2 - 1)^{1/2}} \tag{A6}$$

and the pitch angle at Landau resonance is

$$\cos \alpha_L = \gamma / n_\parallel t \tag{A7}$$

The total spatial growth rate is, of course, $k_i = k_C + k_L$. The gain along a ray path is

$$G = \int_0^s ds\, k_i(s) = \int_0^\lambda r\, d\lambda\, [1 + \tan^2(\psi - \phi - \delta)]^{1/2} k_i(s) \tag{A8}$$

In calculating $k_i(s)$, $j_E{}^*$, M, and N are all functions of L. For $N(L)$ we used the *Kurth et al.* [this issue] density (equation (1)). The power law spectral index is given by

$$\frac{M(L)}{M(L_S)} = 1 + \alpha_M (L - L_S) + \beta_M (L - L_S)^2 \tag{A9}$$

where for $L_S = 6.47$ (7.4), $M(L_S) = 1.75$ (1.87), $\alpha_M = 0.05923$ (-0.5606), and $\beta_M = 0.1945$ (0.53023). The L shell dependence of the energetic electron differential flux is given by

$$\frac{j_E{}^*(L)}{j_E(L_S) b_*{}^{A_E}(L_S)} = 1 + \alpha_F (L - L_S) + \beta_F (L - L_S)^2 \tag{A10}$$

where for $L_S = 6.47$ (7.4), $j_E(L_S) = 1.4 \times 10^{15}$ (7.67×10^{14}), $\alpha_F = -0.447$ (-1.6875), and $\beta_F = -0.0494$ (1.5974).

APPENDIX 2

The parallel velocity for cyclotron resonance is given by

$$\beta_\parallel{}^2 = \frac{\Omega_e{}^2}{\omega_{pe}{}^2} \frac{(b_* - \bar{\omega})^3}{\bar{\omega}} \tag{A11}$$

where Ω_e, ω_{pe} refer to equatorial value, $\bar{\omega} = \omega/\Omega_e$, and b_* is the ratio of the local to the equatorial field strength on a given L shell. In calculating $\bar{D}_{\alpha\alpha}$, $\beta_\parallel$ is held constant. Hence from the resonance condition and whistler group speed we have

$$n = \frac{b_* - \bar{\omega}}{\beta_\parallel \bar{\omega}} \qquad \left| \frac{v_g}{v_g + |v_\parallel|} \right| = \frac{2\bar{\omega}}{b_* + 2\bar{\omega}} \tag{A12}$$

If we let $\bar{\omega}_e$ be the resonant frequency at the equator ($b_* = 1$) for a given $\beta_\parallel$, (A11) can be rewritten as

$$b_*(\bar{\omega}) = \bar{\omega} + (\bar{\omega}/\bar{\omega}_e)^{1/3}(1 - \bar{\omega}_e) \tag{A13}$$

Thus for fixed $\beta_\parallel$, a whistler with frequency $\bar{\omega}$ will be in cyclotron resonance at the location where $b_* = b_*(\bar{\omega})$.

For small magnetic dipole latitudes the relation between the normalized field strength and arc length is

$$b_* = 1 + s^2/s_0{}^2 \qquad s_0{}^2 = \tfrac{2}{5} l^2 R_U{}^2 \tag{A14}$$

Hence $\bar{D}_{\alpha\alpha}$ can be written as

$$\bar{D}_{\alpha\alpha} = \frac{s_0}{2l} \int_1^{b_*(l)} \frac{db_* D_{\alpha\alpha}}{(b_* - 1)^{1/2}} \tag{A15}$$

where $b_*(l) \gg 1$. The observed $E^2(f)$ is strongly peaked at $\bar{\omega}_m = 0.265$ for SCET 2011 ($\bar{\omega}_m = 0.31$ for SCET 2035) and is greatly reduced by the maximum frequency $\bar{\omega}_M = 0.473$ for SCET 2011 ($\bar{\omega}_M = 0.496$ for SCET 2035). Hence we convert the integral over b_* to an integral over $\bar{\omega}$ using the relation (A13) to find

$$\bar{D}_{\alpha\alpha} = \frac{2^{1/2}}{3\pi} \int_{\bar{\omega}_e}^{\bar{\omega}_M} \left\{ d\bar{\omega} \left[1 + \frac{1 - \bar{\omega}_e}{3\bar{\omega}_e{}^{1/3} \bar{\omega}^{2/3}} \right] D_{\alpha\alpha} \cdot [\bar{\omega} - 1 + (\bar{\omega}/\bar{\omega}_e)^{1/3}(1 - \bar{\omega}_e)]^{-1/2} \right\} \tag{A16}$$

where l and s_0 have been substituted. Setting $z = \bar{\omega}/\bar{\omega}_e$ and using (14), (A11), and (A12), $\bar{D}_{\alpha\alpha}$ becomes

$$\bar{D}_{\alpha\alpha} = \frac{1.2 \times 10^4 \omega_{pe}{}^2}{\Omega_e{}^2} \frac{\bar{\omega}_e}{1 - \bar{\omega}_e} \int_1^{\bar{\omega}_M/\bar{\omega}_e} \frac{dz}{z} \cdot \frac{[z^{2/3} + (1 - \bar{\omega}_e)/(3\bar{\omega}_e)] E^2(z)}{[z\bar{\omega}_e - 1 + z^{1/3}(1 - \bar{\omega}_e)]^{1/2} [3\bar{\omega}_e z + z^{1/3}(1 - \bar{\omega}_e)]} \tag{A17}$$

In order to carry out the integral in (A17), we analytically modeled the observed $E^2(f)$ as

$$E^2(\bar{\omega}) = E^2(\bar{\omega}_m) \left[\frac{\bar{\omega}}{\bar{\omega}_m} \right]^{4.75} \exp \left[- \frac{(\bar{\omega}/\bar{\omega}_m - 1)^2}{0.071} \right] \qquad E^2(\bar{\omega}_m) = 6.16 \times 10^{-9}\ \mathrm{V^2/m^2\ Hz} \tag{A18}$$

for SCET 2011 and

$$E^2(\bar{\omega}_m) = E^2(\bar{\omega}_m) \left[\frac{\bar{\omega}}{\bar{\omega}_m} \right]^{1.5} \exp \left[- \frac{|\bar{\omega}/\bar{\omega}_m - 1|^{5/2}}{0.044(\bar{\omega}/\bar{\omega}_m)^{1/4}} \right] \qquad E^2(\bar{\omega}_m) = 2.84 \times 10^{-9}\ \mathrm{V^2/m^2\ Hz} \tag{A19}$$

for SCET 2035. Equation (A18) fits the SCET 2011 spectrum at $\bar{\omega} = 0.147$ and $\bar{\omega} = 0.473$ to within 0.1%. Equation (A19) fits the SCET 2035 spectrum at $\bar{\omega} = 0.23$ and $\bar{\omega} = 0.388$ to within 6% and at $\bar{\omega} = 0.17$ and $\bar{\omega} = 0.496$ to within 15%. The ratio $\omega_{pe}{}^2/\Omega_e{}^2$ equals 24.89 (44.346) for SCET 2011 (SCET 2035).

Acknowledgments. This research was supported at TRW by NASA through contract 954012 with the Jet Propulsion Laboratory, at UCLA by NASA grant NGL-05-007-190, at the University of Iowa by NASA through contracts 954103 and 957723 with the Jet Propulsion Laboratory, and at APL by NASA under Task I of contract N00024-85-C-5300.

The Editor thanks A. Eviatar and two other referees for their assistance in evaluating this paper.

REFERENCES

Bridge, H. S., et al., Plasma observations near Uranus: Initial results from Voyager 2, *Science, 233*, 89, 1986.

Broadfoot, A. L., et al., Ultraviolet spectrometer observations of Uranus, *Science, 233*, 74, 1986.

Burtis, W. J., and R. A. Helliwell, Banded chorus: A new type of VLF radiation observed in the magnetosphere by OGO 1 and OGO 3, *J. Geophys. Res., 74*, 3002, 1969.

Burtis, W. J., and R. A. Helliwell, Magnetospheric chorus: Occurrence patterns and normalized frequency, *Planet. Space Sci., 24*, 1007, 1976.

Cheng, A. F., S. M. Krimigis, B. H. Mauk, E. P. Keath, C. G. Maclennan, L. J. Lanzerotti, M. T. Paonessa, and T. P. Armstrong, Energetic ion and electron phase space densities in the magnetosphere of Uranus, *J. Geophys. Res.*, this issue.

Church, S. R., The generation and distribution of whistler-mode noise in the Earth's plasmasphere, Ph.D. thesis, Univ. of Calif., Los Angeles, 1982.

Church, S. R., and R. M. Thorne, On the origin of plasmaspheric hiss: Ray path integrated amplification, *J. Geophys. Res., 88*, 7941, 1983.

Coroniti, F. V., and C. F. Kennel, Electron precipitation pulsations, *J. Geophys. Res., 75*, 1279, 1970.

Coroniti, F. V., R. W. Fredricks, and R. White, Instability of ring current protons beyond the plasmapause during injection events, *J. Geophys. Res., 77*, 6243, 1972.

Coroniti, F. V., F. L. Scarf, C. F. Kennel, W. S. Kurth, and D. A.

Gurnett, Detection of Jovian whistler mode chorus: Implications for the Io torus aurora, *Geophys. Res. Lett.*, *7*, 45, 1980.

Coroniti, F. V., F. L. Scarf, C. F. Kennel, and W. S. Kurth, Analysis of chorus emissions at Jupiter, *J. Geophys. Res.*, *89*, 3801, 1984.

Gurnett, D. A., W. S. Kurth, F. L. Scarf, and R. L. Poynter, First plasma wave observations at Uranus, *Science*, *233*, 106, 1986.

Inan, U. S., Jovian VLF chorus and Io torus aurora, *J. Geophys. Res.*, *91*, 4543, 1986.

Inan, U. S., R. A. Helliwell, and W. S. Kurth, Terrestrial versus Jovian VLF chorus: A comparative study, *J. Geophys. Res.*, *88*, 6171, 1983.

Kennel, C. F., Consequences of a magnetospheric plasma, *Rev. Geophys.*, *7*, 379, 1969.

Kennel, C. F., and H. E. Petschek, Limit on stably trapped particle fluxes, *J. Geophys. Res.*, *71*, 1, 1966.

Kimura, I., Effects of ions on whistler-mode ray tracing, *Radio Sci.*, *1*, 269, 1966.

Krimigis, S. M., T. R. Armstrong, W. I. Axford, A. F. Cheng, G. Gloeckler, D. C. Hamilton, E. P. Keath, L. J. Lanzerotti, and B. H. Mauk, The magnetosphere of Uranus: Hot plasma and radiation environment, *Science*, *233*, 97, 1986.

Kurth, W. S., D. D. Barbosa, D. A. Gurnett, and F. L. Scarf, Electrostatic waves in the magnetosphere of Uranus, *J. Geophys. Res.*, this issue.

Lyons, L. R., R. M. Thorne, and C. F. Kennel, Pitch angle diffusion of radiation belt electrons within the plasmasphere, *J. Geophys. Res.*, *77*, 3455, 1972.

Mauk, B. H., S. M. Krimigis, E. P. Keath, A. F. Cheng, T. P. Armstrong, L. J. Lanzerotti, G. Gloeckler, and D. C. Hamilton, The hot plasma and radiation environment of the Uranian magnetosphere, *J. Geophys. Res.*, this issue.

McNutt, R. L., R. S. Selesnick, and J. D. Richardson, Low-energy plasma observations in the magnetosphere of Uranus, *J. Geophys. Res.*, *92*, 4399, 1987.

Ness, N. F., M. H. Acuña, K. W. Behannon, L. F. Burlaga, J. E. P. Connerney, R. P. Lepping, and F. M. Neugebauer, Magnetic fields at Uranus, *Science*, *233*, 85, 1986.

Paonessa, M., and A. F. Cheng, Satellite sweeping in offset tilted dipole fields, *J. Geophys. Res.*, *92*, 1160, 1987.

Selesnick, R. S., and R. L. McNutt, Jr., Voyager 2 plasma ion observations in the magnetosphere of Uranus, *J. Geophys. Res.*, this issue.

Stix, T. H,, *The Theory of Plasma Waves*, McGraw-Hill, New York, 1962.

Thorne, R. M., Microscopic plasma processes in the Jovian magnetosphere, in *Physics of the Jovian Magnetosphere*, edited by A. J. Dessler, p. 454, Cambridge University Press, New York, 1983.

Thorne, R. M., and C. F. Kennel, Quasi-trapped VLF propagation in the outer magnetosphere, *J. Geophys. Res.*, *72*, 857, 1967.

F. V. Coroniti, C. F. Kennel, and F. L. Scarf, TRW Space and Technology Group, R1/1176, One Space Park, Redondo Beach, CA 90278.

D. A. Gurnett and W. S. Kurth, Department of Physics and Astronomy, The University of Iowa, Iowa City, IA 52242.

S. M. Krimigis, Applied Physics Laboratory, Johns Hopkins University, Laurel, MD 20707.

(Received March 27, 1987;
revised July 28, 1987;
accepted October 2, 1987.)